Combustion Simulation of 82-Injector Rocket Engine

Juntao Xiong,* Feng Liu,† and William A. Sirignano‡
University of California, Irvine, Irvine, California 92697

https://doi.org/10.2514/1.J061255

A computational study of the nonlinear rocket-engine combustion instability is presented for an engine with 82 coaxial methane–oxygen injector ports, a choked nozzle, and a combustion chamber that models a Rocketdyne experiment. Computations use a three-dimensional unsteady $k-\omega$ shear-stress transport delayed detached-eddy simulation method. Four different one-step chemical kinetic rates are simulated on the resolved scale to determine the effect of the burning rate. Application of kinetic rates on the resolved scale give faster rates than expected with turbulent combustion where the final mixing and chemical reaction in the cascade occurs on the smallest scales; thus, reduction of the kinetic rate is examined here. When the normalized kinetic rate is 1, implying the nominal Westbrook–Dryer rate, only the longitudinal-mode instability is observed. As the kinetic rate decreases, less of the combustion occurs upstream near the longitudinal-mode pressure antinode, the longitudinal-mode instability becomes weak, and the first-tangential-mode instability emerges, which fits better with experiment. The proximity of the domain of major heat release to the longitudinal mode pressure antinode is found to be critical. Evidence is presented for the need for an improved combustion model that will provide a more accurate and lower burning rate.

Nomenclature

A_r	=	normalized chemical kinetic rate
c_p	=	specific heat at constant pressure, J/(kg · K)
D_c	=	diameter of combustor chamber, cm
D_t	=	diameter of nozzle throat, cm
D_{kj}	=	mass diffusivity for species k in j direction, m^2/s
E	=	stagnation internal energy, J
e	=	stagnation specific internal energy, J/kg
H	=	stagnation internal enthalpy, J
HRR	=	heat-release rate, W
h	=	specific enthalpy, J/kg
h_s	=	stagnation specific enthalpy, J/kg
k	=	turbulent kinetic energy, m^2/s^2
L_{chamber}	=	length of combustion chamber
p	=	static pressure, bar
q_i	=	energy flux in ith direction, J/(m^2 · s)
R	=	mixture specific gas constant, J/(kg · K)
R_{ad}	=	radius of chamber, cm
R_{throat}	=	radius of throat, cm
u_i	=	velocity components, m/s
$V_{k,i}$	=	correction velocity for species k in ith direction, m/s
T	=	temperature, K
t	=	time, s
W	=	total molecular weight, kg/mol
W_k	=	molecular weight of species k, kg/mol
X_k	=	mole fraction of species k
x_i	=	position, m
Y_k	=	mass fraction of species k
γ	=	ratio of specific heats
λ	=	total thermal diffusivity, m^2/s
λ_k	=	thermal diffusivity of species k, m^2/s
μ	=	total dynamic viscosity, kg/(m · s)
μ_k	=	dynamic viscosity of species k, kg/(m · s)
μ_t	=	turbulent eddy viscosity, kg/(m · s)
υ_t	=	turbulent kinematic viscosity, kg/(m · s)
ρ	=	mass density, kg/m^3
τ_{ij}	=	shear stress tensor, Pa
ω	=	specific rate of dissipation
ω_k	=	reaction rate of species k, kg/(m^3 · s)

Received 6 September 2021; revision received 17 March 2022; accepted for publication 17 March 2022; published online 19 April 2022.

*Associate Specialist, Department Mechanical and Aerospace Engineering. Member AIAA.

†Professor, Department Mechanical and Aerospace Engineering. Fellow AIAA.

‡Professor, Department Mechanical and Aerospace Engineering. Fellow AIAA.

I. Introduction

COMBUSTION instability in liquid-propellant rocket engines is a phenomenon involving coupling mechanisms between acoustic waves and flames that affect combustion dynamics and combustion instability [1–5]. The acoustic oscillations occur at natural resonant frequencies for the injection–combustor–nozzle configuration and have amplitudes that rise above the level of combustor noise related to vortex shedding. For the combustion instability, flames engage in the resonant interaction and provide oscillatory burning rates that reinforce the acoustic oscillations. Combustion instability has been studied for many decades [2–21] and is considered in all development programs for new rocket designs because it is an undesired and harmful phenomenon; the resulting large-amplitude pressure oscillation can modify the thrust vector and damage the engine through increased heat transfer to the walls and injector face. For liquid-propellant engines, the simulation with the largest number of injectors had 42 coaxial injectors [17]. In that study, Urbano et al. performed large-eddy simulation (LES) for a hydrogen–oxygen liquid-rocket engine with 42 coaxial injectors, addressing two experimental operating conditions investigated at the DLR, German Aerospace Center laboratory. The occurrence of transverse high-frequency combustion instabilities was predicted by superimposing a pressure disturbance with a first transverse modal distribution on the steady-state solution.

Jensen et al. [20] evaluated hydrocarbon fuels, such as methane, with liquid oxygen (LOX) considering combustion stability and performance behavior of a rocket engine with 82 injectors. The first mode of tangential combustion instability with frequency 5100 Hz was observed under some fuel/oxidizer ratio conditions. A previous computational study [21] modeled a rocket engine with 30 coaxial methane–oxygen injector ports, a choked nozzle, and a combustion chamber that is simplified from Jensen et al.'s [20] 82-injector experimental rocket engine. The 30 coaxial injectors were designated to provide a similar mass flux distribution in the radial and azimuthal directions as found for the experimental 82-injector design. The spontaneous longitudinal-mode and tangential-mode instabilities are observed. The strengths of the two instability modes alternate during the simulation time. The oscillation amplitudes of the two instability modes could be modified by pulsing the injector mass flux at certain pulsation frequencies.

In this study, a computational study for a rocket engine with an 82-injector combustor is performed and compared with Jensen et al.'s [20] experimental measurements to understand better the stability of the

reacting flow in a multiple-injection rocket-engine combustor and to develop and validate the computational tool. To reduce the computational cost, the fuel and oxidizer injection geometry is simplified as a coaxial injector port without flare. The open-source computational fluid dynamics software OpenFOAM [22] is used for this study.

The analysis here is a substantial advancement in the complexity of liquid-propellant rocket engine analysis by LES. The three-dimensional flow system configured here includes the internal ports of 82 coaxial injectors, the main combustion chamber, and the transonic flow through the converging–diverging nozzle. The turbulent mixing of the 82 coaxial jets and the one-step methane–oxygen chemical reaction rate are resolved. The LES captures the combustion dynamics due to both the turbulence and the nonlinear acoustics known as combustion instability. In comparison with the previously most advanced configuration for a hydrogen–oxygen rocket engine [17], we have approximately double the number of their 42 coaxial injectors, and we use kinetics rather than the classical flame transfer function, which originated with the Crocco time-lag theory [2,4–8].

In Sec. II, the configuration, mathematical description, and the numerical method are presented. The results of the computations and the postprocessing of that data are given in Sec. III. Section IV contains the concluding remarks.

II. Numerical Method

A. Numerical Solver

In this study, OpenFOAM is used to solve the compressible Navier–Stokes equations, which can be expressed as

$$\frac{\partial \rho}{\partial t} + \frac{\partial(\rho u_j)}{\partial x_j} = 0 \tag{1}$$

$$\frac{\partial(\rho u_i)}{\partial t} + \frac{\partial(\rho u_i u_j)}{\partial x_j} = \frac{\partial(\tau_{ij})}{\partial x_j} - \frac{\partial p}{\partial x_i} \tag{2}$$

$$\frac{\partial(\rho E)}{\partial t} + \frac{\partial(((\rho E) + P)u_j)}{\partial x_j} = \dot{\omega}_T - \frac{\partial q_i}{\partial x_i} + \frac{\partial(\sigma_{ij}u_i)}{\partial x_j} \tag{3}$$

where the viscous stress tensor τ_{ij} is given by

$$\tau_{ij} = \tau_{ij}^L + \tau_{ij}^T \tag{4}$$

$$\tau_{ij}^L = \mu\left(\frac{\partial u_i}{\partial x_j} + \frac{\partial u_j}{\partial x_i}\right) - \frac{2}{3}\mu\frac{\partial u_k}{\partial x_k}\delta_{ij} \tag{5}$$

$$\sigma_{ij} = \tau_{ij} - p\delta_{ij} \tag{6}$$

The detached-eddy simulation [23] model based on the $k-\omega$ shear-stress transport is used for turbulence closure.

The $\dot{\omega}_T$ represents the heat-release rate due to combustion, and q_i represents the energy flux and is given by

$$q_i = -\lambda\frac{\partial T}{\partial x_i} + \rho\sum_{k=1}^{\mathrm{NS}} h_k Y_k V_{k,i} \tag{7}$$

where $V_{k,i}$ represents the diffusion velocity and is defined as

$$V_{k,i} = -\frac{D_k}{X_k}\frac{\partial X_k}{\partial x_i} \tag{8}$$

The species transport equation is

$$\frac{\partial(\rho Y_k)}{\partial t} + \frac{\partial(\rho u_j Y_k)}{\partial x_j} = \frac{\partial}{\partial x_j}\left(\rho D_{kj}\frac{W_k}{W}\frac{\partial X_k}{\partial x_j}\right) + \dot{\omega}_k; \quad k = 1, \ldots, \mathrm{NS} \tag{9}$$

where W_k is the species molecular weight, W is the total molecular weight, D_k is the coefficient of species diffusion, and $\dot{\omega}_k$ is the generation of species due to chemical reaction. The Westbrook–Dryer one-step global reaction [24] for methane and oxygen is used to calculate the generation of species due to chemical reactions and the heat-release rate. No turbulent combustion closure is included. The reacting-mixtures model is used to calculate the properties of the mixtures. More details about the numerical models are given in Ref. [19].

The OpenFOAM 4.0 combustion simulation solver rhoReactingFoam with Pressure Implicit Pressure-Linked Equations (PIMPLE) is used for the compressible combustion simulation with chemical reaction. The Mach number in the combustion chamber is about 0.2. Most combustion are completed in the chamber. The flow is accelerated through the nozzle, and the maximum Mach number there is about 1.4. The differencing schemes used are second-order accurate in both space and time. The time discretization is second-order implicit backward differencing. Gaussian integration is used for the spatial discretization with linear interpolation from cell centers to cell faces for second-order derivatives. It is a standard Gaussian finite volume integration for the derivatives calculations, which is based on summing values on cell faces. The ideal-gas equation of state is used in this paper for simplicity. The specific heat c_p is calculated as a function of temperature from the Joint Army Navy NASA Air Force (JANNAF) tables of thermodynamics.

B. Computational Mesh

An 82-injector rocket engine combustor is configured to mimic an experimental 82-injector rocket engine combustor [20] in this study. Figure 1 shows the 82-injector combustor geometry. P1–P6 mark six pressure probes around the combustion chamber wall. The experiment model [20] had a chamber length of 24 cm, and the combustion chamber diameter is 14.38 cm. In the experiment, 82-element coaxial injectors were used. In the computation model, the injector is simplified as a shorter length without outlet flare coaxial injector. The fuel and oxygen are injected with coaxial injectors. The D_{ox} is 6.62 mm, and D_{fuel} is 7.505 mm. The length of the injector is 30 mm. The 6 deg flare outlet in the experimental geometry is not modeled in the simplified computational model, which might cause some discrepancy between the computation and experiment. Figure 2 shows the combustor geometry. In the simulation, the total mass flow rate and the mixture ratio match those in the experiments. Figure 3 shows the unstructured mesh for the 82-injector combustor. The ANSYS software is used for the mesh

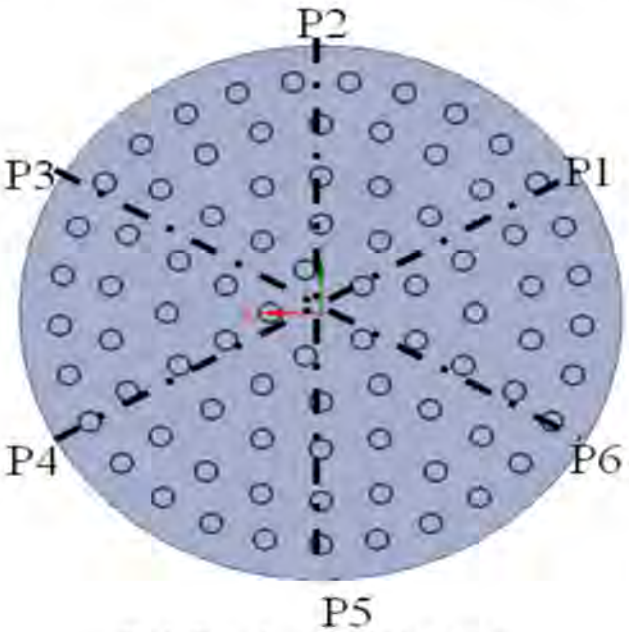

Fig. 1 Front view of the 82-injector plate.

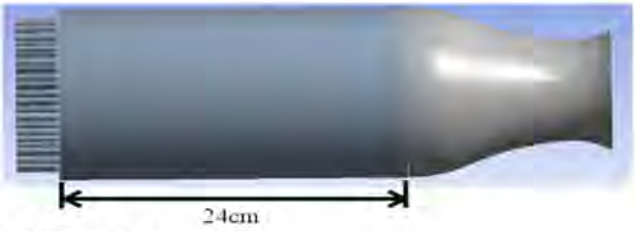

a) Side view of the combustor

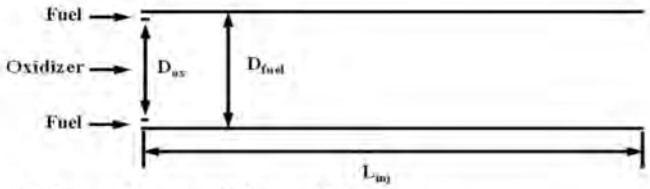

b) Schematic diagram of the coaxial injector

Fig. 2 Geometry of 82-injector combustor.

Fig. 3 Computational mesh.

generation. A grid independency was performed for a combustion chamber with 19-injector case in Ref. [19]. The results show that overall grid independent solutions were achieved on both coarse and fine meshes. In this paper, a fine mesh including about 16.5 million nodes and 50 million elements and a coarse mesh including 8.2 million nodes and 21 million elements are generated for the 82-injector combustion chamber grid independent study.

C. Boundary Conditions

Along the wall, the no-slip boundary condition is used. The normal pressure gradient on the wall is zero. Adiabatic walls with no surface

Table 1 Imposed flow conditions

Data	Case19
Mixture ratio	2.53
Velocity ratio	11.0
Momentum ratio	4.31
$\dot{m}_{fuel}$, lb/s	24.23
$\dot{m}_{LOX}$, lb/s	61.74
T_{fuel}, F	20.7
T_{ox}, F	-244
ρ_{fuel}, lb/ft^3	8.1
ρ_{ox}, lb/ft^3	64.7
V_{fuel}, ft/s	708
V_{ox}, ft/s	64

Table 2 Experimental observations

Content	Case 19
Instability	Tangential
Mode	1T
Frequency, Hz	5100
Chamber pressure, bar	130

Table 3 Combustion chamber characteristic frequencies

Mode	Frequency, Hz
1L	1875
2L	3751
3L	5625
1T	5100
2T	8462
1R	10626

chemistry are assumed. In the injector ports, the mean mass fluxes for methane and oxygen are fixed to yield the steady-state mass flow rate at the sonic point for the convergent nozzle. The wave-transmissive boundary condition is used at the exhaust nozzle outlet boundary because of the supersonic nozzle flow. This boundary condition ensures that no backward propagating waves enter the system to avoid occurrences of shocks or backflow in the combustion. The flow condition is chosen to represent a case with unstable tangential modes based on the experiments. The imposed flow conditions are listed in Table 1. The experimental observations at the conditions are listed in Table 2. The combustion chamber characteristic frequencies are listed in the Table 3. Only the 1st order Tangential mode (1T) instability was found in the test case 19.

III. Computational Results

The simulations only consider the gas phases of the methane and oxidizer and use the ideal-gas equations of state, which might introduce some errors for the description of the cold propellant flow at the very high pressures. The computational simulation results are shown in Table 4. The computational results on the fine and coarse meshes show that overall grid-independent solutions were achieved. Similar combustion chamber pressure level, pressure oscillation frequencies, and instability behaviors were captured on both coarse and fine meshes. However, unlike the Rocketdyne results [20] and 30-injector combustor simulation results [21], only the first longitudinal instability mode with frequency 2403 Hz is observed for the 82-injector combustor when the chemical kinetic rate is 1, normalized by the value given by the Westbrook–Dryer model. [24] The 30-injector combustor studied in Ref. [21] is simplified from the experimental 82-injector combustor in Ref. [20]. The mixing of the 82-injector combustor is faster than the 30-injector combustor, which enhances

Table 4 Parameters of the computation cases

Injector	Ar	Lc, cm	Pc, bar	Longitudinal mode	f_L	Tangential mode	f_T
82	1.0	24	130	1L	2403	— —	— —
82 (coarse)	1.0	24	131	1L	2433	— —	— —
82	0.5	24	125	1L	1918	1T	4657
82	0.375	24	126	1L	1753	1T	4383
82	0.25	24	122	— —	— —	— —	— —
30	1.0	24	125	1L	2063	1T	4550

the combustion rates, moves the combustion upstream in the chamber, and results in only the first longitudinal instability mode appearing for the 82-injector combustor. Three other combustion simulations are tested for the 82-injector combustor with different chemical reaction rates. When the chemical reaction rate is decreased to 0.5, the first tangential instability mode appears, but the first longitudinal instability mode still dominates the pressure oscillation. When the chemical reaction rate is decreased to 0.375, the first tangential instability mode strength grows and dominates the pressure oscillation with frequency 4383 Hz. The smaller reaction rate slows down the combustion in the chamber, which permits the tangential instability to grow. With a further decrease of the combustion reaction rate to 0.25, the flow inside the combustion chamber becomes stable.

The 30-injector simulation involves slower mixing rates than the 82-injector simulation because the distance between adjacent injectors and the sizes of injector ports are larger. The burning rates of the 82-injector simulation and the 30-injector simulation can be aligned closer by artificially reducing the chemical kinetic rate for the 82-injector simulation. This adjustment aligns better the region of major heat-release rate with respect to the pressure antinode of the longitudinal mode. Specifically, the reduced chemical kinetic rate moves the heat-release action farther downstream from the injector plate, weakening the probability of a longitudinal mode without any weakening of the tangential mode.

A. 82-Injector and 30-Injector Combustors

Simulation results are listed in Table 4. The simulations start from an initially quiescent flow at 3000 K and an equilibrium chamber pressure at 200 bar. The higher chamber temperature helps to shorten the ignition process and reduce the computational time without the use of an explicit ignition model in the simulation.

Figure 4 shows the pressure oscillation at six equally distributed probes around the combustor chamber wall at 1 cm downstream from the injection plate for the 82-injector and 30-injector combustors. The

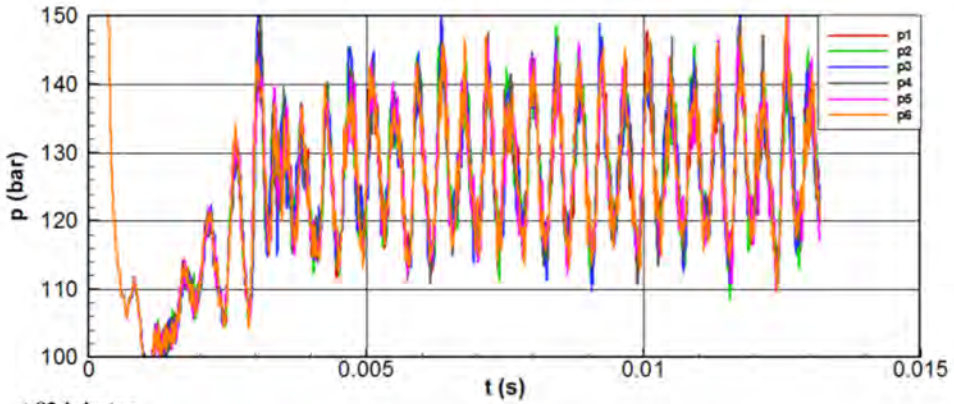

a) 82-injector

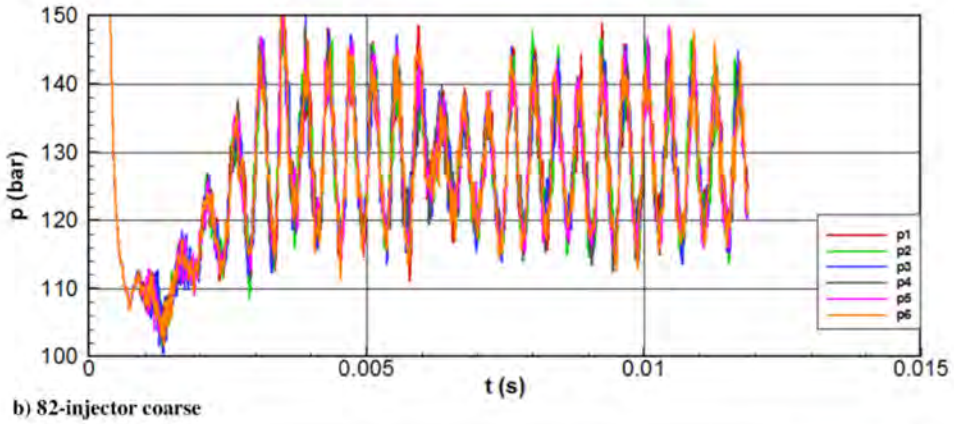

b) 82-injector coarse

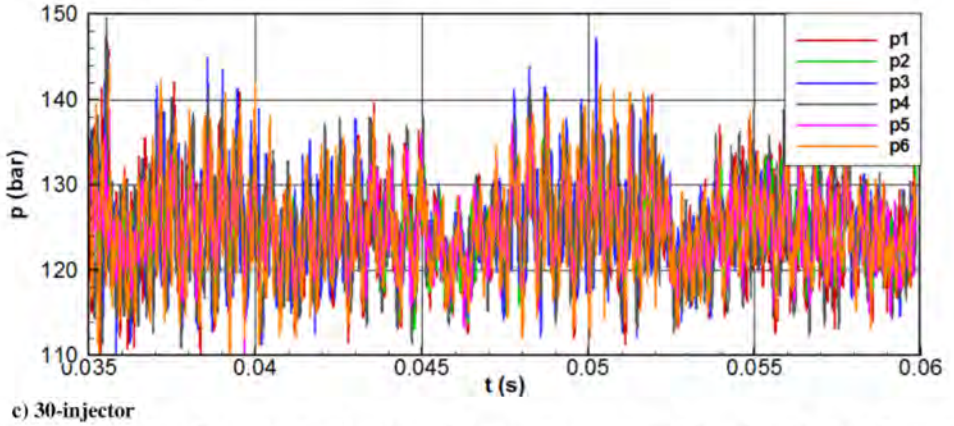

c) 30-injector

Fig. 4 Pressure history at P1–P6 on the combustion-chamber wall for reaction rate Ar = 1 (z = 1 cm). (PSD = Power Spectral Density.)

30-injector combustor is simplified from the 82-injector combustion [21]. The pressure oscillations at the six probes are almost completely in phase for the 82-injector case, while those for the 30-injector case appear to show different phases, indicating a pure longitudinal mode for the 82-injector results, while the 30-injector contains mixed modes. Figure 5 shows the Fast Fourier transform (FFT) analysis of the pressure oscillation at probe 1. The pressure oscillation spectra on the fine and coarse mesh are similar. Both fine and coarse mesh capture the first longitudinal instability mode with 2403 and 2433 Hz, respectively, which confirm the grid independent results are achieved. To contrast the differences, Fig. 5b reproduces the results for the 30-injector study from Ref. [21]. Two dominant frequencies, 2063 and 4550 Hz, are observed for the 30-injector combustor. The 2063 Hz pressure oscillation corresponds to the first longitudinal mode of combustion instability. The 4550 Hz pressure oscillation indicates the first tangential mode. We demonstrate in this study that the discrepancy of the combustion simulation results is caused by the different mixing rates and the reaction rates between the 82-injector and 30-injector combustors.

The higher frequencies for the 82-injector combustion chamber imply a higher speed of sound at the higher temperature, and faster and more complete combustion. This is to be expected because of the shorter mixing lengths and thereby faster mixing rates resulting from the smaller size of injector ports and smaller distances between adjacent injectors.

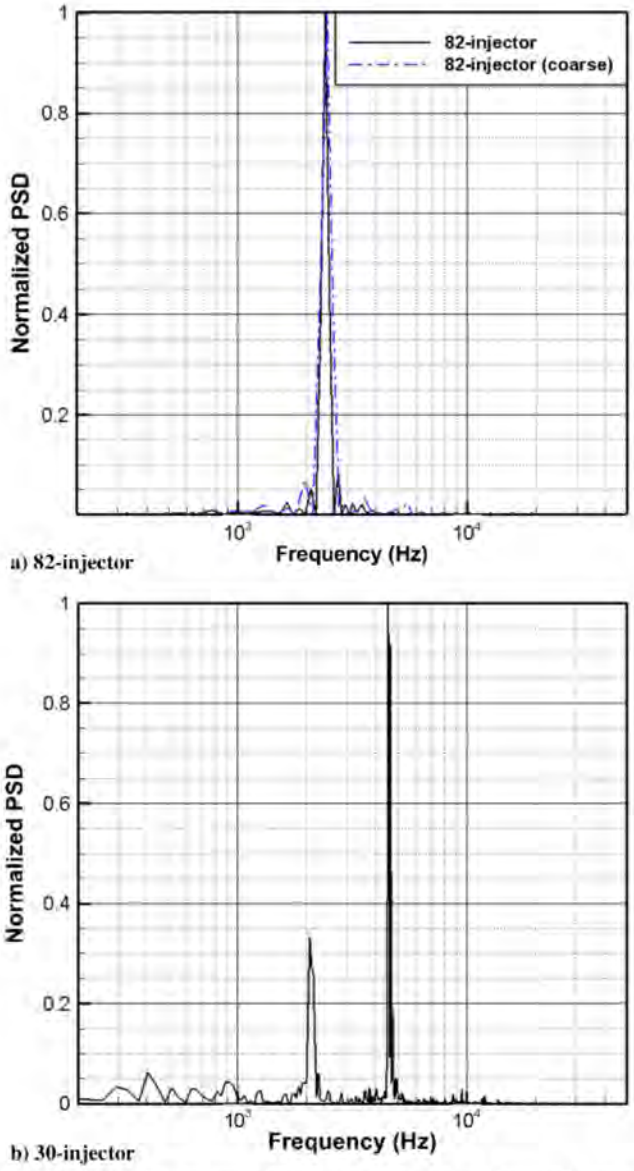

Fig. 5 FFT of the pressure history at probe p1 on the combustion-chamber wall for reaction rate Ar = 1 (z = 1 cm).

B. Chemical Kinetic Rate Effects

Now, we consider the combustion modeling with the different normalized chemical kinetic reaction rates of 0.5, 0.375, and 0.25, respectively. Figure 6 shows the pressure oscillations around the combustor chamber wall at 1 cm downstream from the injection plate for the three cases. The FFT analysis of the pressure oscillations is presented in Fig. 7. When the normalized chemical kinetic reaction rate is 0.5, the first tangential instability mode appears, but the first longitudinal instability mode still dominates the pressure oscillation. When the normalized chemical kinetic reaction rate decreases to 0.375, the first tangential instability mode strength grows and dominates the pressure oscillation with frequency 4383 Hz. With the normalized chemical kinetic reaction rate reaching to 0.25, the flow inside the combustion chamber gradually becomes stable.

Figures 8–11 present the fuel CH4 mass fraction at seven different cross-sections for the 30-injector and the 82-injector combustors with different reaction rates. Figures 12–15 show the product H_2O mass fraction at the same seven different cross-sections. The heat-release rate at meridian plane (1, 0, 0) for the different cases are presented in Fig. 16. For the 82-injector, when the normalized chemical kinetic rate is 1, the combustion mostly happens near the injector plane. The fuel CH_4 is consumed fast. The high heat-release rate near the pressure antinode favors the development of the longitudinal mode inside the combustion chamber. So, only the longitudinal mode is observed. When the normalized chemical kinetic rate decreases, the combustion region moves downstream. As the normalized chemical kinetic rate reaches 0.375, the combustion region moves away from the longitudinal mode pressure antinode point. This move of heating zone favors the tangential mode inside the combustion chamber. The tangential instability mode dominated the pressure oscillation inside the combustion chamber for this case. When the normalized chemical kinetic rate is 0.375 for the 82-injector combustor, the burning rate behavior of the fuel and oxidizer is similar to that of the 30-injector combustor. Thus, the locations of heat release are similar. So, the instability behaviors are similar for the two cases. The distance of high heat-release rate zone from the pressure antinode of the longitudinal mode is critical. Figure 17 presents the instantaneous contours of the flame index on the chamber meridian planes for the chemical kinetic rate 0.375 case. The flame index is defined as the heat-release rate per unit volume masked by the sign of the dot product of the gradient of the oxygen mass fraction and the gradient of the fuel mass fraction, in other words,

$$\mathrm{FI} = \mathrm{HRR} \cdot \mathrm{sign}(\nabla(\mathrm{CH_4})\nabla(\mathrm{O_2})) \tag{10}$$

where HRR is heat-release rate per unit volume. If the index is positive, fuel and oxygen diffuse in the same direction, indicating a premixed flame. If the dot product is negative, the oxygen and fuel diffuse in opposing directions, indicating a diffusion flame. In Fig. 17, the dark red indicates premixed flames, and the dark blue indicates diffusion flames. Premixed flames dominate near the injectors for the case when the chemical kinetic rate is 0.375, which favors the tangential instability.

IV. Conclusions

A computational study of the nonlinear rocket-engine combustion instability is presented for an engine with 82 coaxial methane–oxygen injector ports, a choked nozzle, and a combustion chamber. The analysis is a substantial advancement in the complexity of liquid-propellant rocket engine analysis by large-eddy simulation because of the larger number of coaxial injectors and the use of chemical kinetics rather than a flame transfer function. Use of kinetic rates on the resolved scale gives faster rates than expected with turbulent combustion where the final mixing and chemical reaction in the cascade occurs on the smallest scales; thus, reduction of the kinetic rate is examined here. When the normalized kinetic rate is 1.0, the full

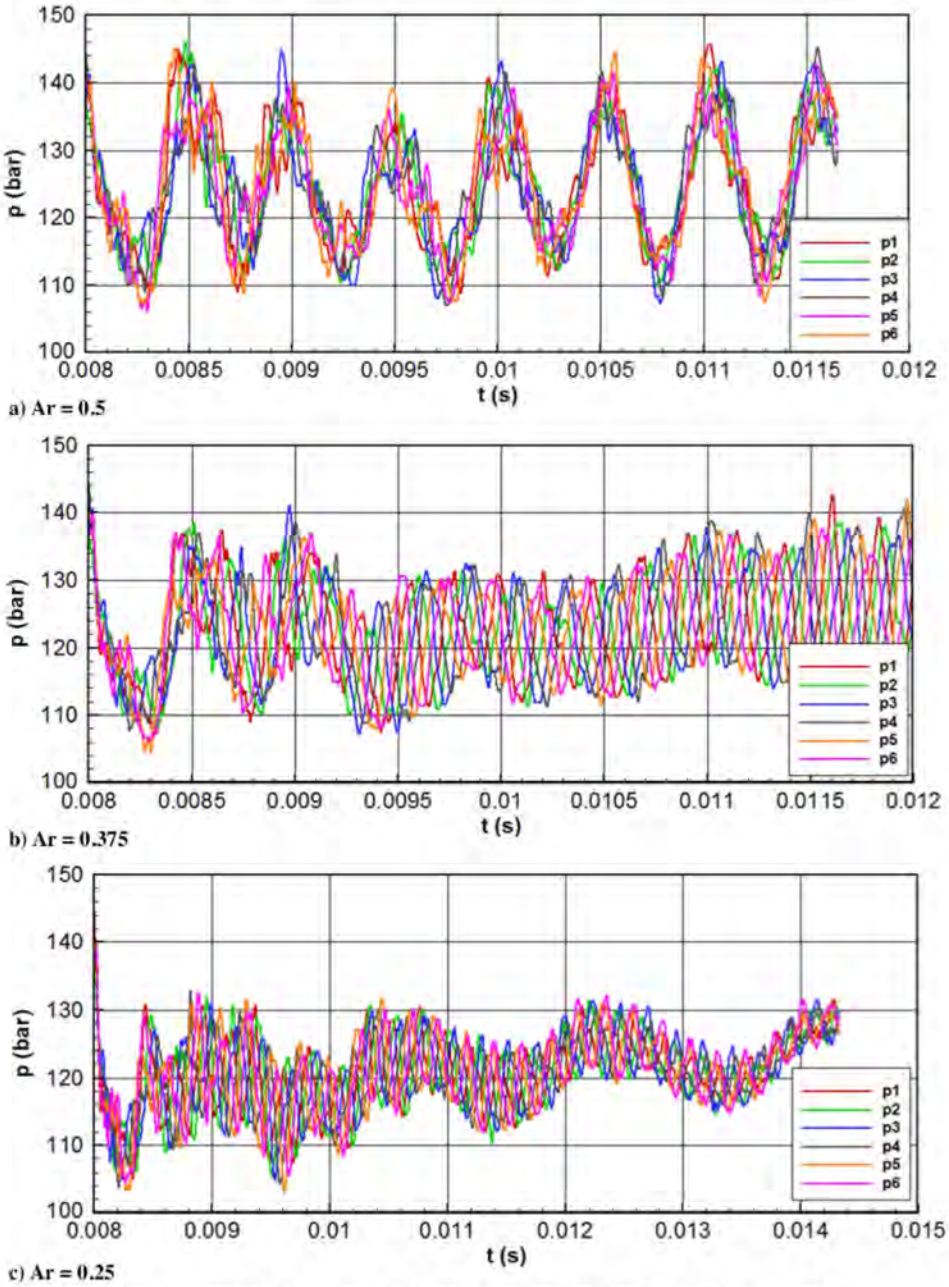

Fig. 6 Pressure history at p1–p6 on the combustion-chamber wall ($z = 1$ cm).

and correct Westbrook–Dryer rate is given; the normalized rates 1.0, 0.5, 0.375, and 0.25 are used in the combustion simulation. When the normalized chemical kinetic rate is 1.0, only the first-longitudinal-mode instability is observed. With reduction of that rate to 0.5, the first-tangential instability mode appears, but the first-longitudinal instability mode still dominates the pressure oscillation. With further reduction of the normalized chemical kinetic rate to 0.375, the first-tangential instability mode strength grows and dominates the pressure oscillation with frequency 4383 Hz. For the normalized chemical kinetic rate equal to 0.25, the flow inside the combustion chamber gradually becomes stable. The different chemical kinetic rates change both the heat-release rate and the location of the heat release, which results in different pressure-oscillation behavior in the combustion chamber. A faster burning rate places more of the heat release at the upstream end of the combustion chamber and thereby closer to the pressure antinode for the longitudinal mode. Thus, it favors the longitudinal instability.

The Rocketdyne experiment [20] indicated the tangential mode was dominant. Agreement with the 82-injector experiment was better with the 30-injector simulation [21] at the same pressure, mass flux, and mixture ratio where the larger mixing lengths reduced the burning rate and moved the heat release farther downstream. This disagreement with experiment for the full chemical rate applied at the resolved scale is not surprising because combustion process actually occurs primarily in the final stage of the turbulent cascade at the smallest scales. We have unpublished evidence [25] in other multi-injector rocket-engine analyses that subgrid modeling with a flamelet-theory approach reduces the burning rate and moves heat release farther downstream in comparison to chemical kinetics applied on the resolved scale. There can be other issues as well related to disagreement with experiment: 1) the Westbrook–Dryer scheme was designed for premixed flames rather than the mixtures of premixed and nonpremixed flames found in a rocket chamber, 2) detailed kinetics might present a slower global rate, 3) mixing rates at high pressure might not be simulated as well as needed, and/or 4) injector-port simulation is not exact, which can modify mixing rates.

Nevertheless, the simulation does present an explanation for some of the instabilities found in the Rocketdyne experiment [20]. Furthermore, the relation of the dominant mode of instability to details in

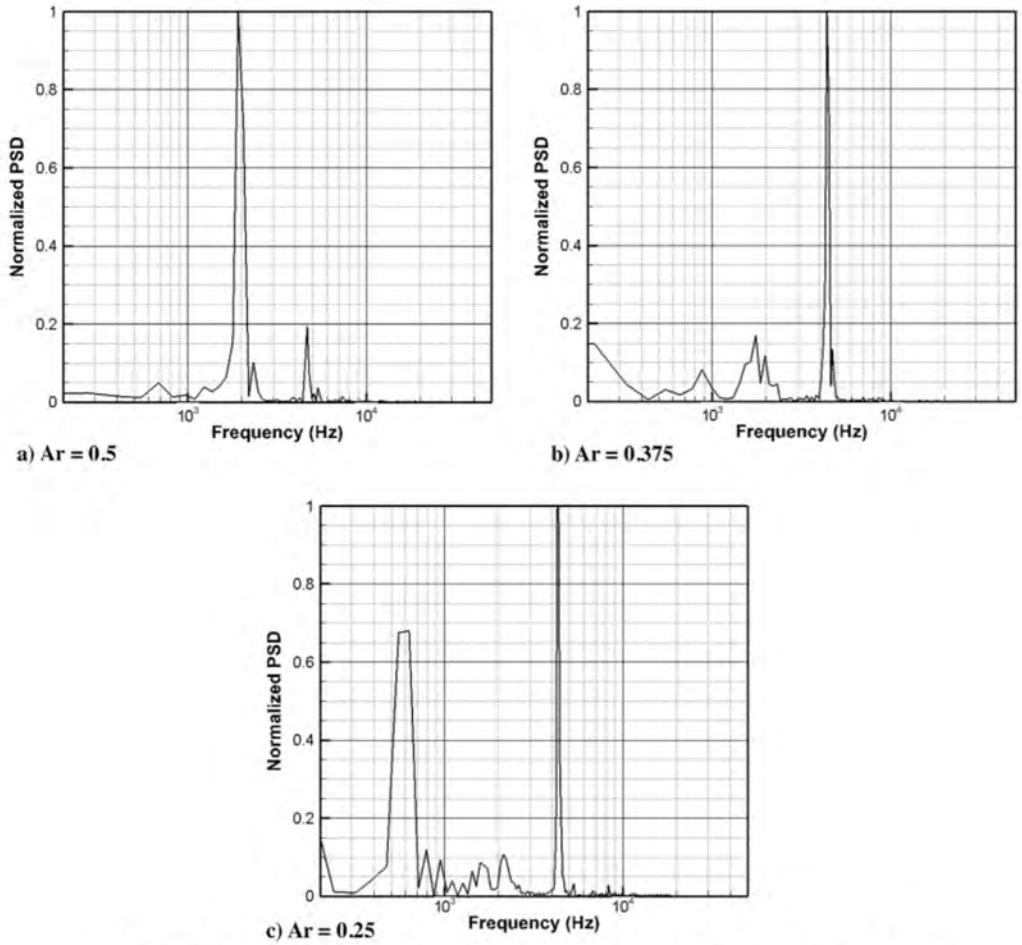

Fig. 7 FFT of the pressure history at probe p1 on the combustion-chamber wall ($z = 1$ cm).

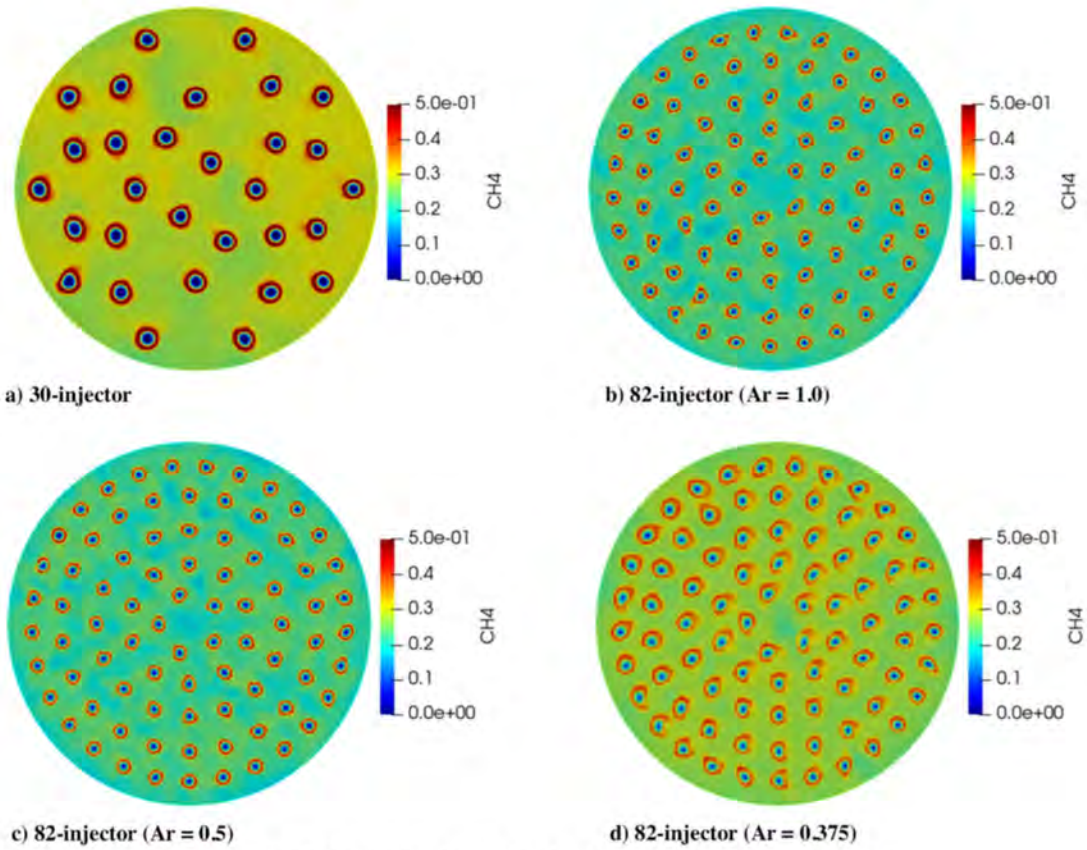

Fig. 8 Fuel CH_4 mass fraction at chamber cross-sectional plane ($z = 1.0$ cm).

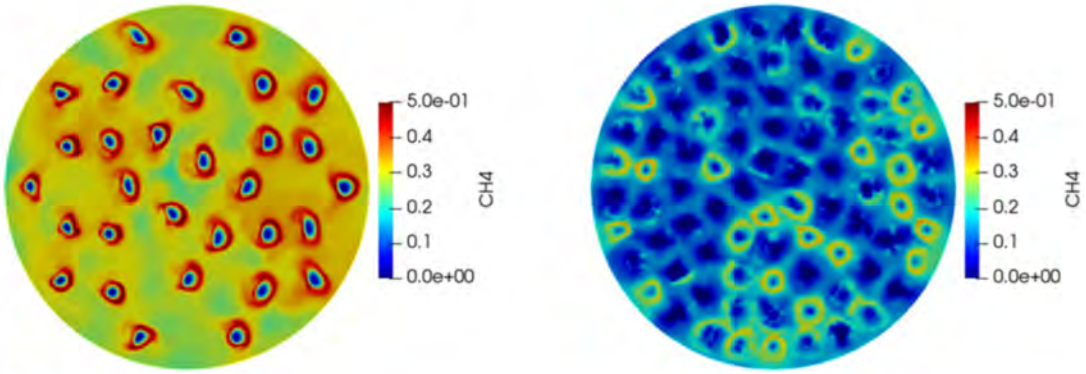

a) 30-injector b) 82-injector (Ar = 1.0)

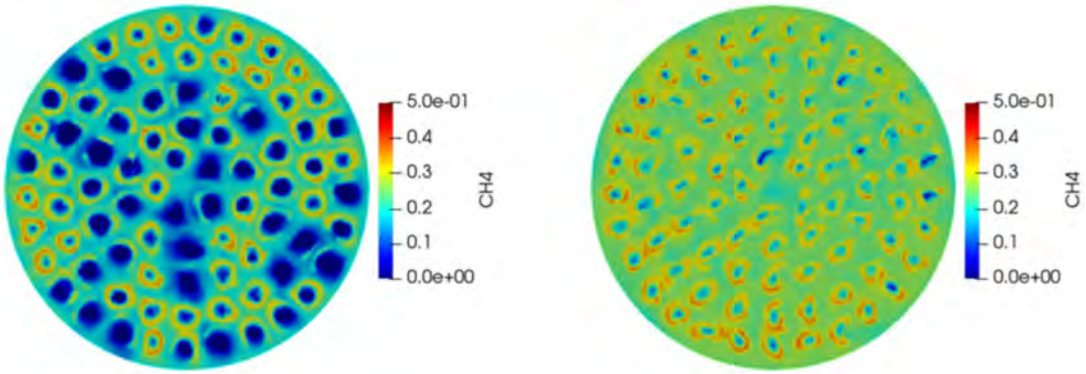

c) 82-injector (Ar = 0.5) d) 82-injector (Ar = 0.375

Fig. 9 Fuel CH_4 mass fraction at chamber cross-sectional plane ($z = 3.0$ cm).

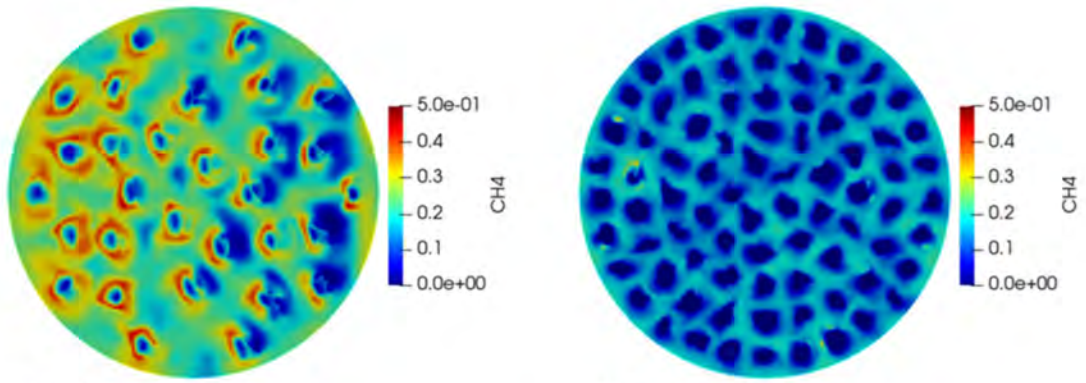

a) 30-injector b) 82-injector (Ar = 1.0)

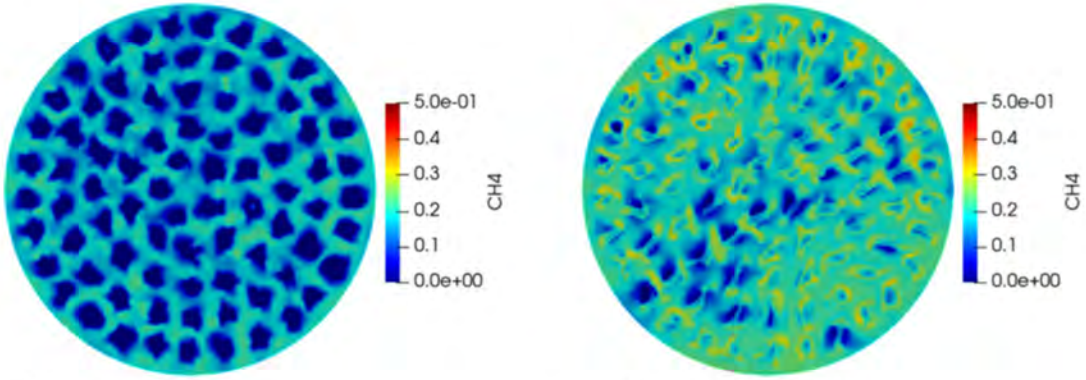

c) 82-injector (Ar = 0.5) d) 82-injector (Ar = 0.375)

Fig. 10 Fuel CH_4 mass fraction at chamber cross-sectional plane ($z = 5.0$ cm).

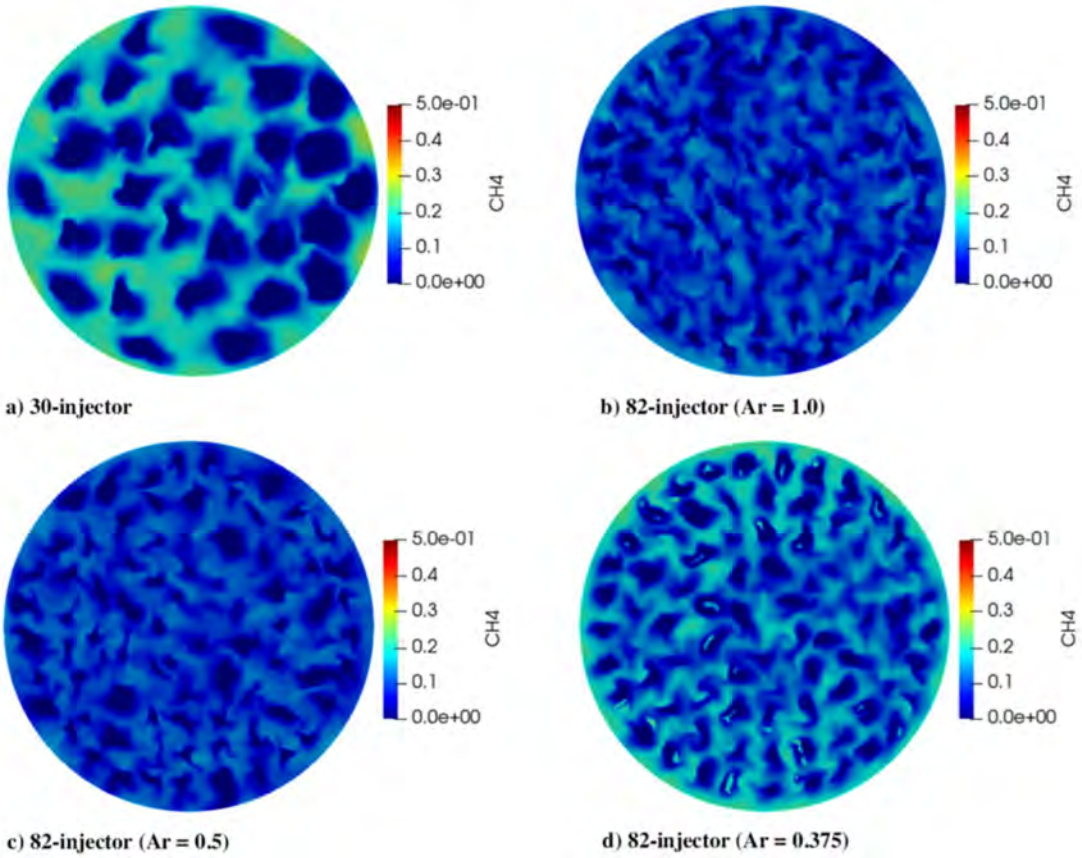

a) 30-injector b) 82-injector (Ar = 1.0)

c) 82-injector (Ar = 0.5) d) 82-injector (Ar = 0.375)

Fig. 11 Fuel CH_4 mass fraction at chamber cross-sectional plane ($z = 10.0$ cm).

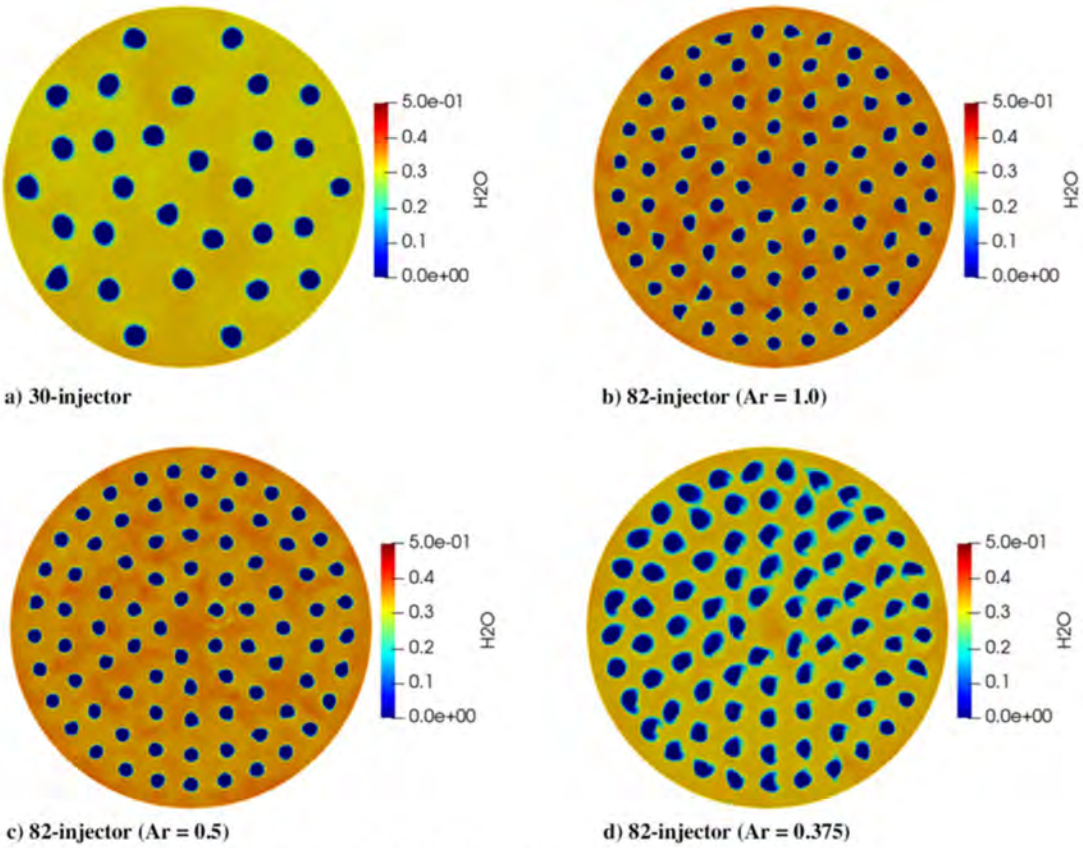

a) 30-injector b) 82-injector (Ar = 1.0)

c) 82-injector (Ar = 0.5) d) 82-injector (Ar = 0.375)

Fig. 12 H_2O mass fraction at chamber cross-sectional plane ($z = 1.0$ cm).

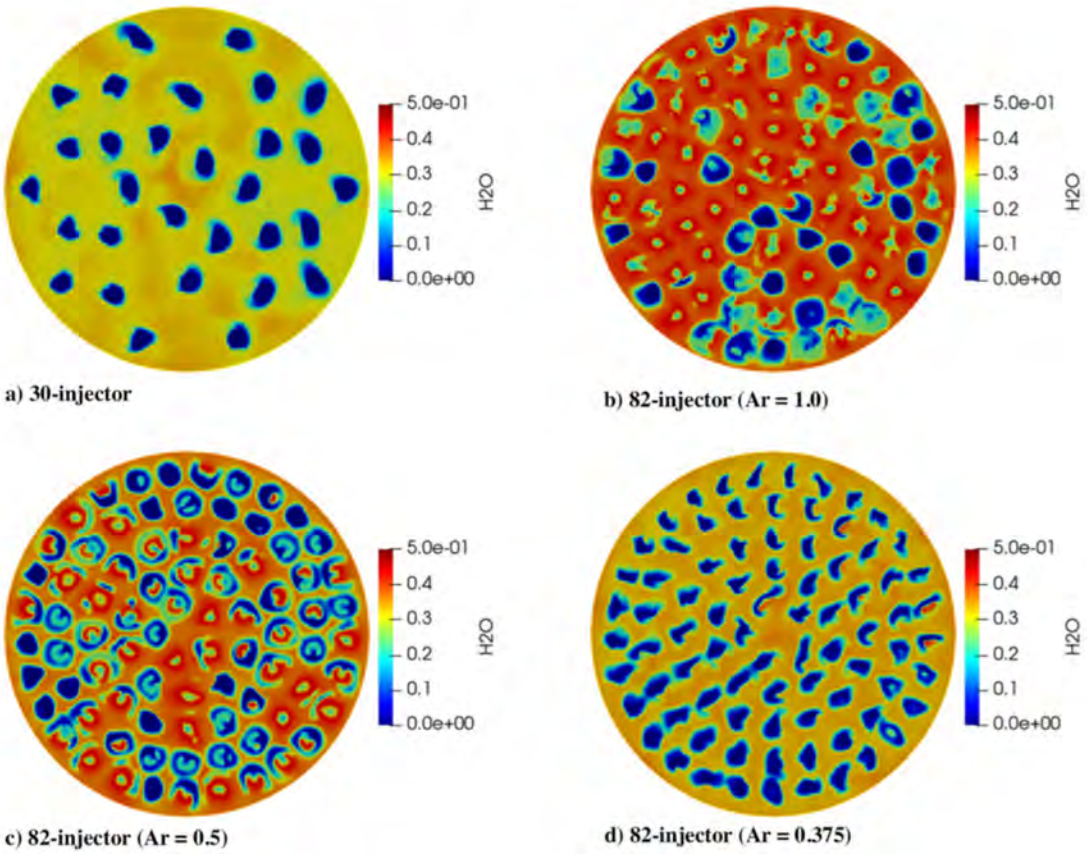

a) 30-injector b) 82-injector (Ar = 1.0)

c) 82-injector (Ar = 0.5) d) 82-injector (Ar = 0.375)

Fig. 13 H_2O mass fraction at chamber cross-sectional plane ($z = 3.0$ cm).

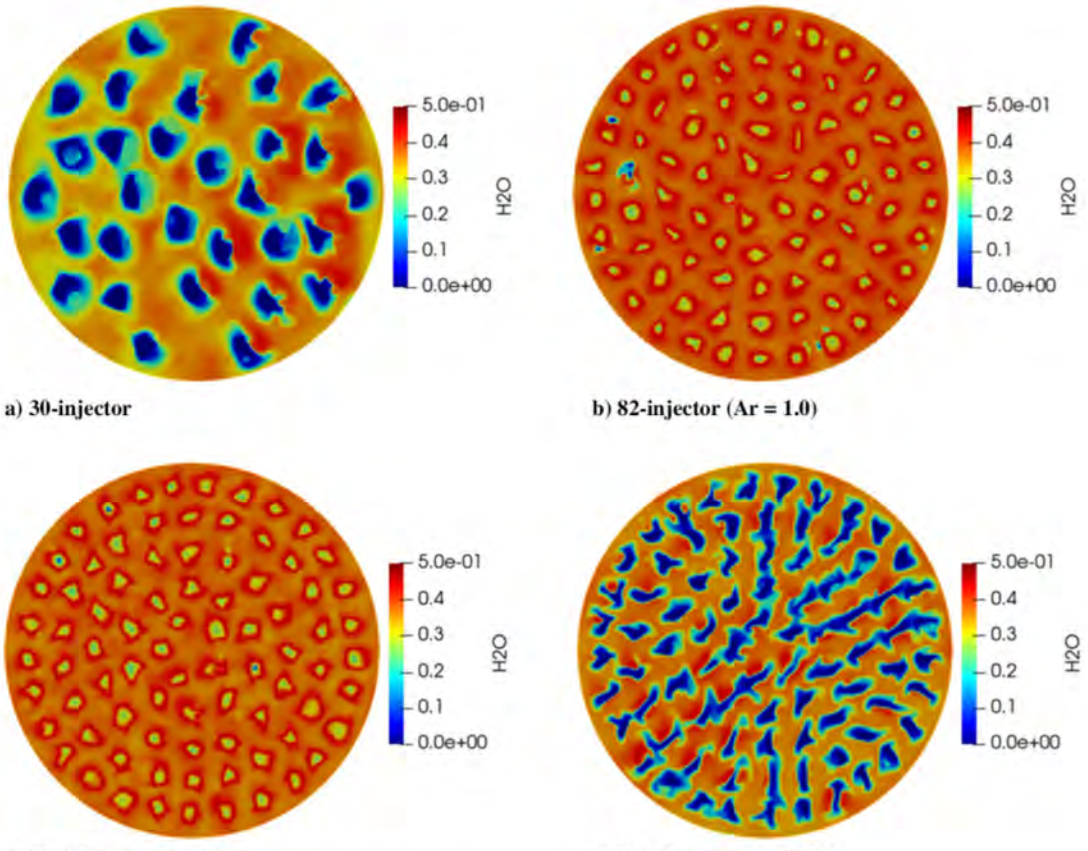

a) 30-injector b) 82-injector (Ar = 1.0)

c) 82-injector (Ar = 0.5) d) 82-injector (Ar = 0.375)

Fig. 14 H_2O mass fraction at chamber cross-sectional plane ($z = 5.0$ cm).

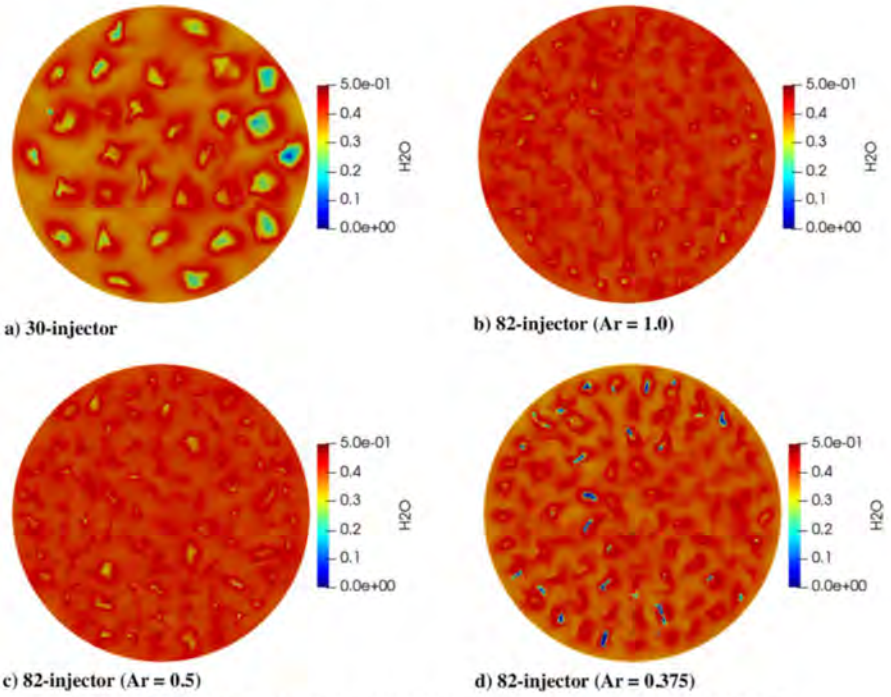

a) 30-injector b) 82-injector (Ar = 1.0)

c) 82-injector (Ar = 0.5) d) 82-injector (Ar = 0.375)

Fig. 15 H_2O mass fraction at chamber cross-sectional plane ($z = 10.0$ cm).

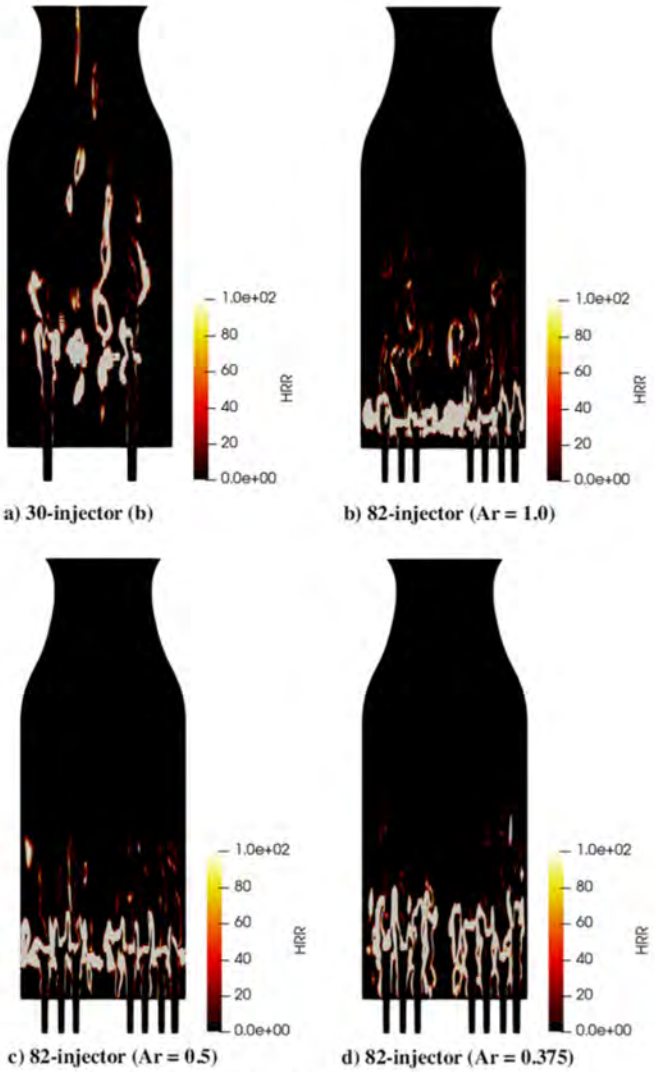

a) 30-injector (b) b) 82-injector (Ar = 1.0)

c) 82-injector (Ar = 0.5) d) 82-injector (Ar = 0.375)

Fig. 16 Heat-release rate at meridian plane (1, 0, 0).

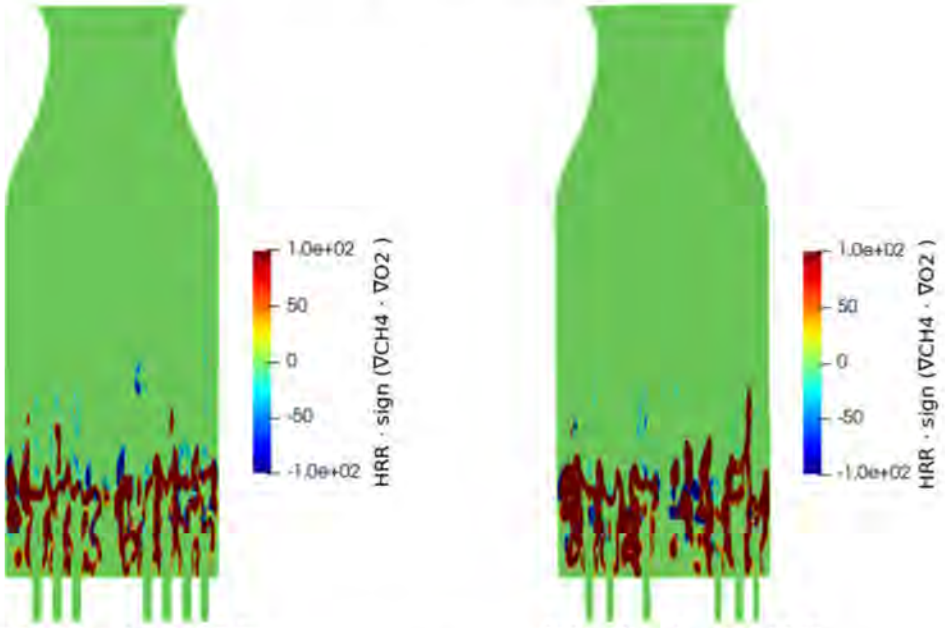

a) Meridian plane 1 (1, 0, 0) b) Meridian plane 1 (1, 1.1, 0)

Fig. 17 Instantaneous flame index on the chamber meridian planes (Ar = 0.375).

the distribution of the heat-release rate has been demonstrated. The simulation demonstrates that the ability exists to address more practical rocket engine combustors with a large number of injectors.

The poor fit of a simple combustion model in providing agreement in the instability-mode prediction indicates the need for an improved combustion model. The success of the flamelet model in matching experimental results for a single-injector rocket engine [10–12,16] suggests that it should be applied to the multi-injector engine. Preliminary work in that direction with a ten-injector engine [25] indicates that the flamelet model gives the desired lower burning rate and favors the transverse mode accordingly.

Acknowledgments

This research was supported by the U.S. Air Force Office of Scientific Research under grant FA9550-18-1-0392, with Mitat Birkan as the Program Manager. The authors also thank Air Force High-performance computing (HPC) for providing the computation resource for the research.

References

[1] Poinsot, T., and Veynante, D., *Theoretical and Numerical Combustion*, 3rd ed., Aquaprint, Bordeaux, France, 2011.

[2] Harrje, D., and Reardon, F., "Liquid Propellant Rocket Combustion Instability," NASA TR SP194, 1972

[3] Oefelein, J. C., and Yang, V., "Comprehensive Review of Liquid-Propellant Combustion Instability in F-1 Engines," *Journal of Propulsion and Power*, Vol. 9, No. 5, 1993, pp. 657–677. https://doi.org/10.2514/3.23674

[4] Crocco, L., and Cheng, S. L., "High Frequency Combustion Instability in Rockets with Distributed Combustion," *4th International Symposium on Combustion*, Vol. 4, The Combustion Inst., 1953, pp. 865–880.

[5] Crocco, L., and Cheng, S. L., "Theory of Combustion Instability in Liquid Propellant Rocket Motors," AGARD, Monograph 8, Neuilly-Sur-Seine, France, 1956.

[6] Sirignano, W. A., and Crocco, L., "A Shock Wave Model of Unstable Rocket Combustors," *AIAA Journal*, Vol. 2, No. 7, 1964, pp. 1285–1296. https://doi.org/10.2514/3.2534

[7] Mitchell, C. E., Crocco, L., and Sirignano, W. A., "Nonlinear Longitudinal Instability in Rocket Motors with Concentrated Combustion," *Combustion Science and Technology*, Vol. 1, No. 1, 1969, pp. 35–64. https://doi.org/10.1080/00102206908952190

[8] Zinn, B. T., "A Theoretical Study of Nonlinear Combustion Instability in Liquid-Propellant Rocket Engines," *AIAA Journal*, Vol. 6, No. 10, 1968, pp. 1966–1972. https://doi.org/10.2514/3.4908

[9] Culick, F. E. C., "Unsteady Motions in Combustion Chambers for Propulsion System," AGARDograph, AG-AVT-039, Neuilly-Sur-Seine, France, 2006.

[10] Nguyen, T. M., and Sirignano, W. A., "The Impacts of Three Flamelet Burning Regimes in Nonlinear Combustion Dynamics," *Combustion and Flame*, Vol. 195, No. 10, 2018, pp. 170–182. https://doi.org/10.1016/j.combustflame.2018.03.031

[11] Miller, K., Sisco, J., Nugent, N., and Anderson, W., "Experimental Study of Combustion Instabilities in a Single-Element Coaxial Swirl Injector," *41st AIAA Joint Propulsion Conference*, AIAA Paper 2005-4298, 2005. https://doi.org/10.2514/6.2005-4298

[12] Sisco, J., Yu, Y., Sankaran, V., and Anderson, W., "Examination of Mode Shapes in an Unstable Model Rocket Combustor," *Journal of Sound and Vibration*, Vol. 330, No. 1, 2011, pp. 61–74. https://doi.org/10.1016/j.jsv.2010.07.016

[13] Popov, P. P., Sideris, A., and Sirignano, W. A., "Stochastic Modeling of Transverse Wave Instability in a Liquid-Propellant Rocket Engine," *Journal of Fluid Mechanics*, Vol. 745, 2014, pp. 62–91. https://doi.org/10.1017/jfm.2014.96

[14] Popov, P. P., Sirignano, W. A., and Sideris, A., "Propellant Injector Influence on Liquid-Propellant Rocket Engine Instability," *Journal of Propulsion and Power*, Vol. 31, No. 1, 2015, pp. 320–331. https://doi.org/10.2514/1.B35400

[15] Oefelein, J. C., and Yang, V., "Modeling High-Pressure Mixing and Combustion Processes in Liquid Rocket Engines," *Journal of Propulsion and Power*, Vol. 14, No. 5, 1998, pp. 843–857. https://doi.org/10.2514/2.5349

[16] Nguyen, T. M., Popov, P. P., and Sirignano, W. A., "Longitudinal Combustion Instability in a Rocket Engine with a Single Coxial Injector," *Journal of Propulsion and Power*, Vol. 34, No. 2, 2018, pp. 354–373. https://doi.org/10.2514/1.B36516

[17] Urbano, A., Selle, L., Staffelbach, G., Cuenot, B., Schmitt, T., Ducruix, S., and Candel, S., "Exploration of Combustion Instability Triggering Using Large Eddy Simulation of a Multiple Injector Liquid Rocket Engine," *Combustion and Flame*, Vol. 169, July 2016, pp. 129–140. https://doi.org/10.1016/j.combustflame.2016.03.020

[18] Menon, S., and Jou, W.-H., "Large-Eddy Simulations of Combustion Instability in an Axisymmetric Ramjet Combustor," *Combustion Science and Technology*, Vol. 75, Nos. 1–3, 1991, pp. 53–72. https://doi.org/10.1080/00102209108924078

[19] Xiong, J. T., Morgan, H., Krieg, J., Liu, F., and Sirignano, W. A., "Nonlinear Combustion Instability in a Multi-Injector Rocket Engine," *AIAA Journal*, Vol. 58, No. 1, 2020, pp. 219–235. https://doi.org/10.2514/1.J058036

[20] Jensen, R. J., Dodson, H. C., and Claflin, S. E., "LOX/Hydrocarbon Combustion Instability Investigation," NASA CR-182249, 1989.

[21] Xiong, J. T., Liu, F., and Sirignano, W. A., "Combustion Dynamics Simulation of a 30-Injector Rocket Engine," *Combustion Science and Technology*, 2020, pp. 1–29. https://doi.org/10.1080/00102202.2020.1847097

[22] Weller, H. G., Tabor, G., Jasak, H., and Fureby, C., "A Tensorial Approach to Computational Continuum Mechanics Using Object-Oriented Techniques," *Computers in Physics*, Vol. 12, No. 6, 1998, pp. 620–631. https://doi.org/10.1063/1.168744

[23] Strelets, M., "Detached Eddy Simulation of Massively Separated Flows," *39th AIAA Aerospace Sciences Meeting*, AIAA Paper 2001-0879, 2001. https://doi.org/10.2514/6.2001-879

[24] Westbrook, C. K., and Dryer, F. L., "Chemical Kinetic Modeling of Hydrocarbon Combustion," *Progress in Energy and Combustion Science*, Vol. 10, 1984, pp. 1–57.

[25] Zhan, Lei, Nguyen, T. M., Xiong, J. T., Liu, F., and Sirignano, W. A., "Combustion Instability of a Multi-Injector Rocket Engine Using the Flamelet Progress Variable," https://arxiv.org/abs/2108.12046

Y. Ju
Associate Editor